Letter Vol. 47, No. 24 / 15 December 2022 / Optics Letters 6309

Design of ultracompact broadband focusing spectrometers based on diffractive optical networks

Yilin Zhu,[1] Yuyao Chen,[2] and Luca Dal Negro[1,2,3,*]

[1]Division of Materials Science and Engineering, Boston University, 15 Saint Mary's Street, Brookline, Massachusetts 02246, USA
[2]Department of Electrical and Computer Engineering and Photonics Center, Boston University, 8 Saint Mary's Street, Boston, Massachusetts 02215, USA
[3]Department of Physics, Boston University, 590 Commonwealth Avenue, Boston, Massachusetts 02215, USA
*Corresponding author: dalnegro@bu.edu

Received 9 September 2022; revised 24 October 2022; accepted 11 November 2022; posted 14 November 2022; published 2 December 2022

We propose the inverse design of ultracompact, broadband focusing spectrometers based on adaptive diffractive optical networks (a-DONs). Specifically, we introduce and characterize two-layer diffractive devices with engineered angular dispersion that focus and steer broadband incident radiation along predefined focal trajectories with the desired bandwidth and nanometer spectral resolution. Moreover, we systematically study the focusing efficiency of two-layer devices with side length $L = 100\ \mu m$ and focal length $f = 300\ \mu m$ across the visible spectrum and demonstrate accurate reconstruction of the emission spectrum from a commercial superluminescent diode. The proposed a-DONs design method extends the capabilities of efficient multi-focal diffractive optical devices to include single-shot focusing spectrometers with customized focal trajectories for applications to ultracompact spectroscopic imaging and lensless microscopy.

https://doi.org/10.1364/OL.475375

Compact spectrometers play an important role in many research areas, such as in the analysis of materials, the detection of biological cells, the characterization of light sources, and the rapid determination of chemical species [1]. In particular, the design and fabrication of ultracompact micron-size spectrometers capable to match the microscopic nature of the investigated objects is being extensively investigated [2–12]. There are currently several grating-based ultracompact spectrometer devices, such as on-chip digital planar holographic gratings [5,6], arrayed waveguide gratings (AWGs) [2,3], as well as dispersion-engineered metasurfaces and phase-modulated diffractive axilens devices [7–13]. Additionally, designs based on randomly scattering spectrometers [14], chirped filament-array gratings [15], wavelength-selective filters [16,17], and resonator-based spectrometers [18–20] were also recently proposed. However, these structures face challenges when considering on-demand, non-conventional responses, such as customized focal trajectories, due to the limited flexibility of traditional design approaches.

Recently, the advancement of data-driven machine learning techniques in optics and photonics has offered novel opportunities for inverse design [21–25]. In particular, it led to the development of efficient all-optical diffractive optical networks (DONs) for the engineering of multi-layered devices that are directly trained, based on the definition of a suitable loss function, using error backpropagation without the need of training datasets [26]. This fruitful combination of deep learning methods and diffractive physics has provided abundant degrees of freedom (DOFs) to enable design and prototyping of task-specific, on-demand devices [27–29] based on multi-layer diffractive optical elements (DOEs). Since the first demonstration in object classification [26], DONs have been used for the design of different optical elements, including broadband filters [27], terahertz pulse shapers [28], and dual-band ultracompact focusing lenses [29].

In this paper, we introduce the design of ultracompact diffractive focusing spectrometers based on DONs augmented by adaptive training, called adaptive DONs (a-DONs) [29]. The targeted spectrometers consist of two diffractive layers trained to angularly disperse and focus broadband incident light onto different spatial positions that form desired trajectories on the detection plane. We study the focusing efficiency and bandwidths of such devices and examine the mapping from wavelengths to the focal spot positions. We also investigate how discretized phase and thickness profiles affect the overall focusing efficiency, guiding future device fabrication. Finally, as a proof-of-concept application, we demonstrate the successful reconstruction of the spectrum of a commercial superluminescent diode source.

In Fig. 1, we show the schematics of the designed ultracompact spectrometer consisting of two diffractive square layers acting as unit-amplitude phase plates separated by a distance d. As a concrete implementation, we considered devices with side length $L = 100\ \mu m$, inter-layer separation $d = 250\ \mu m$, and a minimum pixel size $\Delta x = 200$ nm, which is chosen to be compatible with current diffractive optics and doublet metasurface fabrication technology [8,11,30–35]. The two diffractive layers are discretized into 500×500 square pixels. Recent work in achromatic and multi-spectral metasurface technology has shown the ability to engineer wavelength dispersion and correct for chromatic phase aberrations across a sizable portion of the visible spectrum using dielectric coupled nanostructures [36–38]. Motivated by the recent technological advances in dispersion engineering [7,13,31,36], we train an a-DON that

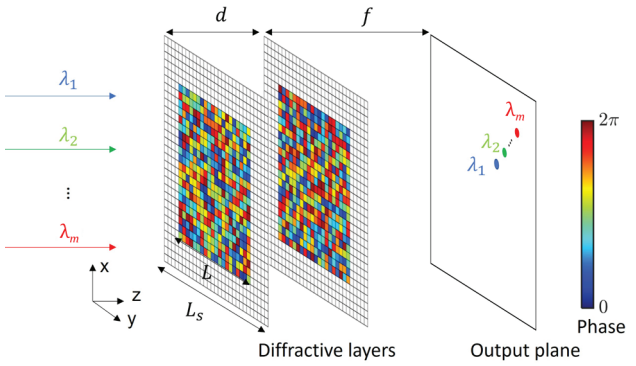

Fig. 1. Schematics of inverse design of ultracompact spectrometer device by a-DON. The device consists of two diffractive layers and is trained over the phase value of each pixel (phase-only modulation unit). The number of pixels on layers is reduced for visualization purpose. Color coding on diffractive layers represents the phase values.

optimizes the phase value ϕ with respect to the loss function defined below. Moreover, to account explicitly for chromatic aberrations, we also considered a design with wavelength-dependent phase values accomplished by training the latent variable h_ℓ [27–29]. This strategy produces definite thickness profiles for both layers of the device (see Supplement 1). We trained the latent variable h_ℓ related to the material thickness of each pixel in the diffractive layers using both a sigmoid and a sine activation function, where $h = h_{\max}\varphi(h_\ell)$ and φ identifies the chosen model (sigmoidal or sinusoidal), and $h_{\max} = 500$ nm is the maximum thickness of the device (see Supplement 1).

Plane waves, with evenly spaced wavelengths $\lambda_1, \lambda_2, \ldots \lambda_m$ over a broad spectral range, centered at λ_0, i.e., $\lambda_0 = (\lambda_1 + \lambda_m)/2$, are used for coherent illumination. These incident waves propagate through the two diffractive layers, then are focused and angularly deflected onto a common output focal plane at a focal distance $f = 300$ μm at desired transverse positions $(x_1, y_1), (x_2, y_2), \ldots, (x_m, y_m)$. The phase plates are zero-padded around their perimeter in the simulation window (L_s as in Fig. 1) to obtain more accurate diffraction field results from the Rayleigh–Sommerfeld (RS) first integral formulation [8,29]:

$$A_o(x', y') = A_s(x, y) * h(x, y; x', y'; z, k), \tag{1}$$

$$h(x, y; z, k) = \frac{1}{2\pi}\frac{z}{r}\left(\frac{1}{r} - jk\right)\frac{e^{jkr}}{r}, \tag{2}$$

where $r = \sqrt{x^2 + y^2 + z^2}$ and z stands for the axial distance between A_o and A_s planes. Note that the two phase plates in Fig. 1 are located on both sides of a transparent substrate with refractive index $n = 3$, as in [29].

The RS integral given in Eqs. (1) and (2) is used to calculate fields at each layer in the a-DON as well as at the output plane. We then introduce the loss function $\mathcal{L}$ defined in terms of the focusing efficiency $\hat{\eta}$. The focusing efficiency $\hat{\eta}$ is the ratio between the power of the focused spot and that of the incident wave. For each incident wavelength λ_i and focal spot position (x_i, y_i), we define $\hat{\eta}$ as [29]

$$\hat{\eta}(\lambda_i, f; x_i, y_i) = \frac{\int_0^{3\mathrm{FWHM}/2} \mathrm{d}\rho_s' \int_0^{2\pi} \mathrm{d}\theta_s'\, I'\left(\lambda_i, z = d + f, \rho_s', \theta_s'\right)}{\iint \mathrm{d}S\, I(\lambda_i, z = 0, \rho, \theta)}. \tag{3}$$

Here in Eq. (3), the full width at half maximum FWHM $= 0.51\lambda_i f/L$ and (ρ_s', θ_s') denote the polar coordinates on the focal plane with its origin shifted to the point (x_i, y_i). So we have $\rho_s' = \sqrt{(x' - x_i)^2 + (y' - y_i)^2}$ and $\theta_s' = \cos^{-1}[(x' - x_i)/\rho_s']$, where (x', y') is the Cartesian coordinates across the focal plane. The relations above show how the focal position (x_i, y_i) gets incorporated in the efficiency calculation and eventually into the loss function $\mathcal{L}$. According to standard grating theory, the angular dispersion of spectrometer devices is quantified by the resolving power, which is given by [1]

$$L(\mathrm{d}\theta/\mathrm{d}\lambda) = \frac{\lambda_0}{\Delta\lambda}, \tag{4}$$

where $\Delta\lambda$ is the minimum resolvable wavelength (i.e., the spectral resolution) of the spectrometer. We adapt the methodology in [8] to distribute the focal positions (x_i, y_i) at wavelengths λ_i along a line with a given direction angle α (with respect to the x axis) on the focal plane. Considering the case of linear angular dispersion, the relation between the focal positions and the wavelengths can be obtained as follows:

$$x_i = \cos\alpha \frac{\lambda_0 f}{L\Delta\lambda}(\lambda_i - \lambda_1) + x_1, \tag{5}$$

$$y_i = \sin\alpha \frac{\lambda_0 f}{L\Delta\lambda}(\lambda_i - \lambda_1) + y_1. \tag{6}$$

Note that these coordinates are the targeted focal positions at the incident wavelengths, and are incorporated into the loss function $\mathcal{L}$ for its minimization. Following this approach, we used the stochastic gradient descent (SGD) method to minimize the loss function in the backpropagation steps. During each epoch, we randomly select B wavelengths from $\lambda_1, \lambda_2, \ldots \lambda_m$ (B<m) as a mini-batch and feed them into the network. Crucially, to improve the convergence, we implemented adaptive loss weights that update along with each loss term during an epoch [29]. The loss function for this mini-batch is thus defined as

$$\mathcal{L} = \sum_{i \in B} w_i \left[1 - \hat{\eta}(\lambda_i, f; x_i, y_i)\right]^2, \tag{7}$$

where w_i is the adaptive loss weight that corresponds to λ_i. These weights are updated with a learning rate γ. They are initialized as unity and updated during the kth epoch based on the following rule [29]:

$$w_i^k \leftarrow w_i^{k-1} + \gamma\left[1 - \hat{\eta}(\lambda_i, f; x_i, y_i)\right]^2. \tag{8}$$

During training, we set the object spectral resolution to be $\Delta\lambda = 5$ nm, which is significantly improved compared to what was previously reported using ultracompact modulated axilenses [8–10]. We sampled $m = 200$ incident wavelengths evenly spaced in the range from $\lambda_1 = 400$ nm to $\lambda_m = 800$ nm, which corresponds to the spectral range of visible light. Given the focal position coordinates of the starting wavelength λ_1 denoted as (x_1, y_1), the positions of the other wavelengths are determined using Eqs. (5) and (6) for a given resolving power. The batch size is selected as $B = 5$. We applied the uniform random initialization for the phase values of each pixel at the beginning of the training. The a-DON is trained over 2000 epochs using the Adam optimizer with a learning rate equal to 0.1. The learning rate for updating adaptive weights are set to $\gamma = 1$. Our deep learning algorithm is developed within the flexible TensorFlow framework. The training is conducted using a Tesla P100

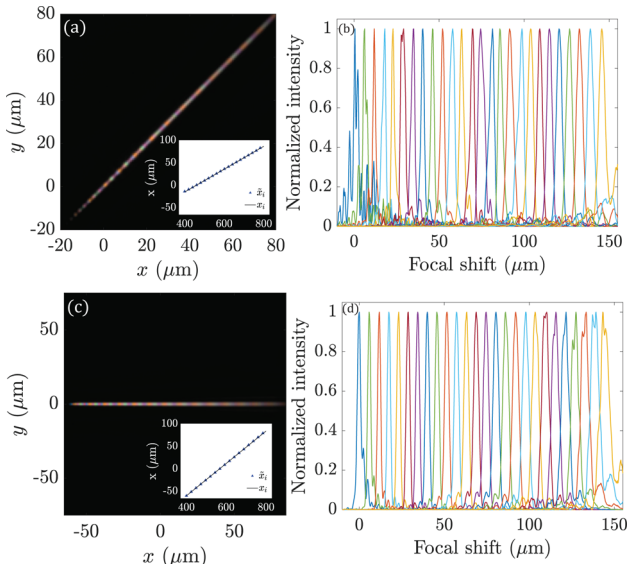

Fig. 2. Simulated intensity profiles (false color image) of the incident wavelengths focused on the $z = 300$-μm focal plane. Focal spots are distributed along the direction angles (a) $\alpha = 45°$, (c) $\alpha = 0°$. Insets in panels (a) and (c) show x coordinates of focal spots (blue triangle markers) and the target focal spots (black solid line). Also shown are normalized intensity line shapes for different wavelengths at the focal plane evaluated with (b) $\alpha = 45°$ line-trajectory and (d) $\alpha = 0°$ line-trajectory. The increment of wavelengths in panels (b) and (d) is 20 nm.

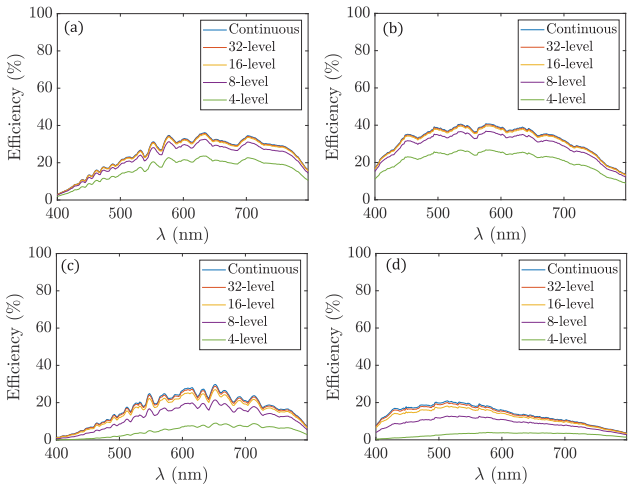

Fig. 3. Focusing efficiency spectra for $\alpha = 45°$ diagonal line with respect to (a) phase and (b) thickness training using a sigmoid function. Focusing efficiency spectra for $\alpha = 0°$ horizontal line with respect to (c) phase and (d) thickness training using sigmoid function. Averaged values of the spectra are displayed corresponding to 10 different initialization conditions of the a-DONs.

graphic processing unit (GPU, Nvidia Inc.) on the Boston University Shared Computing Cluster (SCC). The typical training time is ∼ 10 minutes.

At the end of the training, we obtain devices with a two-layer phase or thickness profiles that achieve the desired spectral resolution $\Delta\lambda$ for a given pixel size Δx. Therefore, the inverse design of ultracompact spectrometers based on a-DONs allows us to target different values of $\Delta\lambda$ independently of Δx, thus reducing the complexity of the manufacturing process. Moreover, we can control the focusing trajectories along the horizontal and vertical directions, thus making the spectrometer capable of dispersing incident wavelengths onto any arbitrary two-dimensional path in the focusing plane.

As an example, in Figs. 2(a) and 2(c), we show the simulated focal plane intensity distributions along a $\alpha = 45°$ diagonal line and a $\alpha = 0°$ horizontal line respectively, while in Figs. 2(b) and 2(d), we show the line shapes of the normalized intensity along the corresponding directions. The incident wavelengths all separate from each other with a 5-nm spacing, which corresponds to the $\Delta\lambda$ used in our proof-of-concept design. Note that we used false colors to better visualize the intensity distributions with respect to each wavelength. It can be clearly observed that the focal spots of the incident wavelengths are well separated on the focal plane. We also examined the dispersion behavior of the focal spots, which are located by finding the positions of local maxima of each intensity distribution with respect to the incident wavelength. The insets in Figs. 2(a) and 2(c) show the comparison between the focal spot positions simulated by forward propagation within a-DON and those given by Eqs. (5) and (6), demonstrating an excellent agreement. These results demonstrate that our device can focus multiple incident wavelengths simultaneously and diffract them onto distinct transverse positions on the same focal plane. By setting different directions of the angular dispersion, we show the capability to map the wavelengths onto positions distributed on arbitrary trajectories.

We then characterize the focusing behavior of the spectrometer device by first evaluating the simulated focusing efficiency spectrum $\hat{\eta}$ in Fig. 3 with respect to the two angular dispersion directions and training methods introduced above. We note that $\hat{\eta}$ shows a broad spectrum with peak efficiency equal to approximately 40% and 30% for phase and thickness training, respectively. Practical fabrication technology, such as that used in DOEs and metasurface engineering, requires the discretization of the phase profile into multiple levels. The impact of phase discretization of the device performances is also shown by the curves with different colors in Fig. 3, where we show the focusing efficiency spectra for different numbers of discrete phase levels. The results demonstrate that an 8-level device already approaches the ideal performance of that of the continuous phase.

Finally, we demonstrate that our multi-layer ultracompact spectrometer device can be used for the single-shot spectral reconstruction of a practical light source. Particularly, we used 8-level discretized devices to reflect the actual fabrication needs. We first calibrated the spectral response of the device using the blackbody radiation as a reference source. The blackbody emission spectrum is given by Planck's law as

$$S_{\text{ref}}(\lambda, T) = \frac{2hc^3}{\lambda^5} \frac{1}{e^{\frac{hc}{kT\lambda}} - 1}, \tag{9}$$

where we considered $T = 5000\,\text{K}$ without loss of generality. The blackbody spectrum in the target spectral region is shown in Fig. 4(a). After calibration, we simulated the spatial intensity distributions for both the blackbody reference and the target source (QSDM-680-2 superluminescent diode, QPhotonics LLC), which are shown in Figs. 4(b) and 4(c), respectively. We denoted these intensity distributions as $I_{\text{ref}}(x', y')$ and $I(x', y')$, respectively. Using Eqs. (5) and (6), we then established a one-to-one mapping between the spatial distributions of the

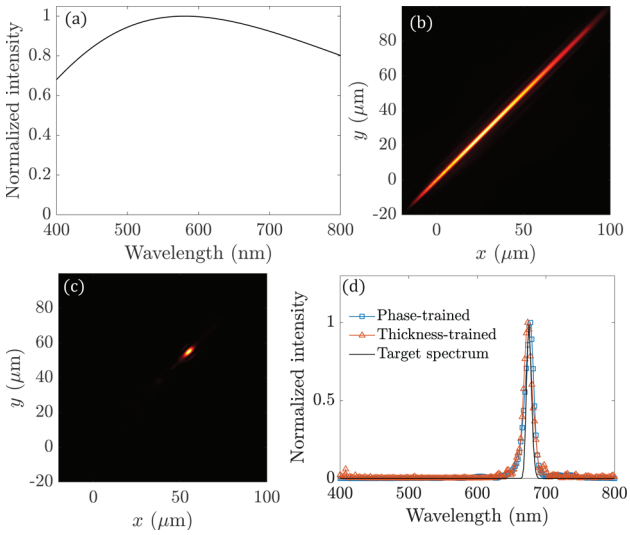

Fig. 4. (a) Blackbody emission spectrum in the range of 400–800 nm. (b) Simulated intensity distribution at $z = 300$ μm when the device is illuminated with a blackbody reference source. (c) Simulated intensity distribution at the same focal plane when the device is illuminated by a superluminescent diode. (d) Reconstructed spectrum of the target diode (black solid line) source via the phase-trained device (blue square markers) and the thickness-trained device (red triangle markers) using the sigmoid model for the h_ℓ training.

intensities and the corresponding spectral distributions (i.e., $I_{\text{ref}}(\lambda)$ and $I(\lambda)$), for a given direction of the angular dispersion (i.e., $\alpha = 45°$ in Fig. 4). The emission spectrum of the diode is finally reconstructed via the following formula [8]:

$$S(\lambda) = I(\lambda)\frac{S_{\text{ref}}(\lambda)}{I_{\text{ref}}(\lambda)}. \tag{10}$$

The reconstruction of the diode spectrum obtained from Eq. (10) matches very well the target curve in Fig. 4(d).

To conclude, we proposed an inverse design approach based on a-DONs for ultracompact spectrometers trained to maximize the focusing efficiency over a broad band of wavelengths with customized focal trajectories. In particular, we demonstrated that the focusing efficiency spectra peaked at around 40% and 30% across the visible and a spectral resolution $\Delta\lambda = 5$ nm for devices with $L = 100$-μm side length. Moreover, the proposed concepts can naturally be extended to spectral bands other than visible. In combination with dispersion-engineered metasurfaces, the flexible a-DON approach introduced here for the design of ultracompact focusing spectrometers enables novel broadband diffractive devices with desired angular and spatial dispersion for applications to multispectral imaging, multi-band detection, and lensless microscopy.

Funding. National Science Foundation (ECCS-2015700).

Disclosures. The authors declare no conflicts of interest.

Data availability. Data underlying the results presented in this paper are not publicly available at this time but may be obtained from the authors upon reasonable request.

Supplemental document. See Supplement 1 for supporting content.

REFERENCES

1. W. Demtröder, *Laser Spectroscopy 1: Basic Principles* (Springer, 2014).
2. J.-J. He, B. Lamontagne, A. Ge, L. Erickson, M. Davies, and E. S. Koteles, J. Lightwave Technol. **16**, 631 (1998).
3. S. Janz, A. Balakrishnan, S. Charbonneau, P. Cheben, M. Cloutier, A. Delâge, K. Dossou, L. Erickson, M. Gao, P. Krug, B. Lamontagne, M. Packirisamy, M. Pearson, and D.-X. Xu, IEEE Photonics Technol. Lett. **16**, 503 (2004).
4. X. Ma, M. Li, and J.-J. He, IEEE Photonics J. **5**, 6600807 (2013).
5. S. Babin, A. Bugrov, S. Cabrini, S. Dhuey, A. Goltsov, I. Ivonin, E.-B. Kley, C. Peroz, H. Schmidt, and V. Yankov, Appl. Phys. Lett. **95**, 041105 (2009).
6. C. Peroz, C. Calo, A. Goltsov, S. Dhuey, A. Koshelev, P. Sasorov, I. Ivonin, S. Babin, S. Cabrini, and V. Yankov, Opt. Lett. **37**, 695 (2012).
7. A. Y. Zhu, W.-T. Chen, M. Khorasaninejad, J. Oh, A. Zaidi, I. Mishra, R. C. Devlin, and F. Capasso, APL Photonics **2**, 036103 (2017).
8. W. A. Britton, Y. Chen, F. Sgrignuoli, and L. Dal Negro, ACS Photonics **7**, 2731 (2020).
9. Y. Chen, W. A. Britton, and L. Dal Negro, Appl. Opt. **59**, 5532 (2020).
10. Y. Chen, W. A. Britton, and L. Dal Negro, Opt. Lett. **45**, 2371 (2020).
11. W. A. Britton, Y. Chen, F. Sgrignuoli, and L. Dal Negro, Laser Photonics Rev. **15**, 2000207 (2021).
12. M. Khorasaninejad, W. T. Chen, J. Oh, and F. Capasso, Nano Lett. **16**, 3732 (2016).
13. A. Y. Zhu, W. T. Chen, J. Sisler, K. M. A. Yousef, E. Lee, Y.-W. Huang, C.-W. Qiu, and F. Capasso, Adv. Opt. Mater. **7**, 1801144 (2019).
14. B. Redding, S. F. Liew, R. Sarma, and H. Cao, Nat. Photonics **7**, 746 (2013).
15. A. Rahnama, K. Mahmoud Aghdami, Y. H. Kim, and P. R. Herman, Adv. Photonics Res. **1**, 2000026 (2020).
16. A. Emadi, H. Wu, G. de Graaf, and R. Wolffenbuttel, Opt. Express **20**, 489 (2012).
17. A. Li and Y. Fainman, Nat. Commun. **12**, 2704 (2021).
18. A. Sharkawy, S. Shi, and D. W. Prather, Appl. Opt. **40**, 2247 (2001).
19. A. Nitkowski, L. Chen, and M. Lipson, Opt. Express **16**, 11930 (2008).
20. Z. Xia, A. A. Eftekhar, M. Soltani, B. Momeni, Q. Li, M. Chamanzar, S. Yegnanarayanan, and A. Adibi, Opt. Express **19**, 12356 (2011).
21. D. Liu, Y. Tan, E. Khoram, and Z. Yu, ACS Photonics **5**, 1365 (2018).
22. W. Ma, Z. Liu, Z. A. Kudyshev, A. Boltasseva, W. Cai, and Y. Liu, Nat. Photonics **15**, 77 (2021).
23. Z. Liu, D. Zhu, L. Raju, and W. Cai, Adv. Sci. **8**, 2002923 (2021).
24. M. Zandehshahvar, Y. Kiarashinejad, M. Zhu, H. Maleki, T. Brown, and A. Adibi, ACS Photonics **9**, 714 (2022).
25. P. R. Wiecha, A. Arbouet, C. Girard, and O. L. Muskens, Photonics Res. **9**, B182 (2021).
26. X. Lin, Y. Rivenson, N. T. Yardimci, M. Veli, Y. Luo, M. Jarrahi, and A. Ozcan, Science **361**, 1004 (2018).
27. Y. Luo, D. Mengu, N. T. Yardimci, Y. Rivenson, M. Veli, M. Jarrahi, and A. Ozcan, Light: Sci. Appl. **8**, 112 (2019).
28. M. Veli, D. Mengu, N. T. Yardimci, Y. Luo, J. Li, Y. Rivenson, M. Jarrahi, and A. Ozcan, Nat. Commun. **12**, 37 (2021).
29. Y. Chen, Y. Zhu, W. A. Britton, and L. Dal Negro, Opt. Lett. **47**, 2842 (2022).
30. S. Banerji, M. Meem, A. Majumder, F. G. Vasquez, B. Sensale-Rodriguez, and R. Menon, Optica **6**, 805 (2019).
31. P. Lalanne and P. Chavel, Laser Photonics Rev. **11**, 1600295 (2017).
32. M. Khorasaninejad, W. T. Chen, R. C. Devlin, J. Oh, A. Y. Zhu, and F. Capasso, Science **352**, 1190 (2016).
33. N. Yilmaz, A. Ozdemir, A. Ozer, and H. Kurt, J. Opt. **21**, 045105 (2019).
34. A. Martins, J. Li, B.-H. V. Borges, T. F. Krauss, and E. R. Martins, Nanophotonics **11**, 1187 (2022).
35. D. Mengu, Y. Luo, Y. Rivenson, and A. Ozcan, IEEE J. Sel. Top. Quantum Electron. **26**, 3700114 (2020).
36. W. T. Chen, A. Y. Zhu, and F. Capasso, Nat. Rev. Mater. **5**, 604 (2020).
37. W. T. Chen, A. Y. Zhu, V. Sanjeev, M. Khorasaninejad, Z. Shi, E. Lee, and F. Capasso, Nat. Nanotechnol. **13**, 220 (2018).
38. Y. Li, X. Li, M. Pu, Z. Zhao, X. Ma, Y. Wang, and X. Luo, Sci. Rep. **6**, 19885 (2016).